npj | quantum information

Article

Published in partnership with The University of New South Wales

https://doi.org/10.1038/s41534-025-01111-z

Experimental verification of threshold quantum state tomography on a fully-reconfigurable photonic integrated circuit

Eugenio Caruccio[1], Diego Maragnano[2], Giovanni Rodari[1], Davide Picus[1], Giovanni Garberoglio[3], Daniele Binosi[3], Riccardo Albiero[4], Niki Di Giano[4,5], Francesco Ceccarelli[4], Giacomo Corrielli[4], Nicolò Spagnolo[1], Roberto Osellame[4] ✉, Maurizio Dapor[3] ✉, Marco Liscidini[2] ✉ & Fabio Sciarrino[1] ✉

Reconstructing the state of a quantum system represents a pivotal task for quantum information applications. The standard approach based on quantum state tomography requires a number of measurements that scales exponentially with the number of qubits. Other methods have been proposed and tested to reduce the number of measurements, or to focus on specific properties of the output state rather than on its complete reconstruction. Here, we show experimentally the application of an approach, called threshold quantum state tomography, in an advanced hybrid photonic platform with states up to $n = 4$ qubits. This method does not require prior knowledge and selects only the informative projectors starting from the measurement of the density matrix diagonal. We demonstrate its effectiveness by showing that a consistent reduction in the number of measurements is obtained for relevant states, with only very limited loss of information. These results open perspective for its application in larger systems.

The ability to accurately characterize a quantum state is a fundamental requirement for the development of quantum technologies. In quantum computing, quantum communication, and quantum metrology, precise knowledge of the state of a system enables the verification of quantum protocols, the validation of experimental implementations, and the assessment of device performance. However, obtaining a complete description of a quantum state is a challenging task. A general quantum state is represented by its density matrix, which encodes all the relevant statistical properties of the system. In principle, knowing this matrix provides access to any observable quantity. Yet, reconstructing the density matrix from experimental data using quantum state tomography (QST) requires performing a series of measurements, whose number scales exponentially with the system size[1–4].

As quantum platforms advance towards higher-dimensional states and larger numbers of qubits, dealing with this exponential scaling is crucial in quantum information science. While the constraints of laboratory resources, including measurement time and computational capabilities, limit the feasibility of QST, alternative strategies have been developed to mitigate this issue. Compressed sensing QST, for example, reduces the number of required measurements by leveraging prior assumptions on the rank of the density matrix[5–7]. Bayesian QST, in contrast, introduces probabilistic models to optimize measurement selection[8–10]. Other approaches, such as shadow tomography, aim to extract relevant information while avoiding full-state reconstruction[11–13].

An alternative strategy is represented by threshold quantum state tomography (tQST)[14]. The core idea behind tQST is to exploit the structure of the density matrix to prioritize the most significant measurements. Specifically, it leverages the fact that the off-diagonal elements of a density matrix are constrained by the diagonal ones, allowing for a systematic reduction in the number of required measurements. The protocol follows a simple sequence: first, the diagonal elements of the density matrix are measured on the given computational basis; second, a threshold parameter is introduced to determine which off-diagonal elements are likely to contribute significantly; finally, only those selected elements are measured, and the density matrix is reconstructed based on this reduced dataset. By adjusting the threshold, tQST provides a tunable balance between measurement effort and reconstruction accuracy. This can lead to a significant reduction of measurements, particularly for systems where the density matrix is naturally sparse.

[1]Dipartimento di Fisica, Sapienza Università di Roma, Roma, Italy. [2]Dipartimento di Fisica, Università di Pavia, Pavia, Italy. [3]European Centre for Theoretical Studies in Nuclear Physics and Related Areas (ECT* Fondazione Bruno Kessler), Villa Tambosi, Villazzano, TN, Italy. [4]Istituto di Fotonica e Nanotecnologie, Consiglio Nazionale delle Ricerche (IFN-CNR), Milano, Italy. [5]Dipartimento di Fisica, Politecnico di Milano, Milano, Italy. ✉e-mail: roberto.osellame@cnr.it; dapor@ectstar.eu; marco.liscidini@unipv.it; fabio.sciarrino@uniroma1.it

While tQST has been successfully demonstrated in superconducting qubit systems[14], extending its application to photonic platforms represents an important step toward broader applicability, as these systems offer unique advantages in terms of scalability, coherence properties, and compatibility with integrated architectures[15,16]. In this work, we experimentally validate tQST in a photonic system based on single photons generated from a quantum dot source and manipulated within a femtosecond laser-written integrated circuit. This platform combines high-performance photon generation with fully-reconfigurable photonic processing capabilities, making it well-suited for scalable quantum information processing. Photonic qubits encoded in spatial and polarization modes provide a flexible framework for implementing high-dimensional quantum states, enabling an exploration of tQST in a regime distinct from previous demonstrations in superconducting circuits.

The rest of this manuscript is structured as follows. In Section "Theoretical background", we provide the theoretical background of QST and introduce the principles of tQST, outlining its advantages and operational framework. In Section "Experimental apparatus", we describe the experimental setup, detailing the photonic platform used to implement the protocol. Section "Experimental results" presents the results of our experimental validation, analyzing its effectiveness for different classes of quantum states. Finally, we summarize in the "Discussions" our findings and discuss potential directions for future research.

Results

Theoretical background

QST aims to reconstruct the representation of a quantum state by measuring a sufficiently large number of observables. In this work, we consider the density matrix as the representation of quantum states, i.e., a trace-one, Hermitian, and positive semi-definite matrix. The number of required observables is determined by the dimension of the density matrix. Specifically, for a system of n qubits, in principle $4^n - 1$ observables are necessary, corresponding to the number of independent real parameters characterizing the density matrix. One can perform the measurements in any order, and subsequently process the acquired data using appropriate statistical inference methods, such as maximum likelihood estimation or Bayesian mean estimation[1,8].

The properties of density matrices, particularly positive semi-definiteness, impose constraints on their off-diagonal elements ρ_{ij}, specifically that $|\rho_{ij}| \leq \sqrt{\rho_{ii}\rho_{jj}}$. Consequently, measuring the diagonal elements provides information about the off-diagonal ones. For example, if ρ_{ii} is zero, then all elements in the i-th row and column of ρ must also be zero. Similarly, if ρ_{ii} and ρ_{jj} are non-zero but small relative to other diagonal elements, the modulus of ρ_{ij} will also be small.

These observations form the basis of the tQST protocol, which we now describe[14]. The protocol (schematically shown in Fig. 1) consists of the following steps: (i) we first directly measure the diagonal elements $\{\rho_{ii}\}$ of the density matrix by projecting onto the elements of the chosen computational basis; (ii) we choose a threshold t, and using the information from $\{\rho_{ii}\}$, the off-diagonal elements ρ_{ij} satisfying $\sqrt{\rho_{ii}\rho_{jj}} \geq t$ are identified; (iii) a set of projectors providing information on these selected ρ_{ij} elements is constructed, and we perform only these measurements; (iv) finally, we process the measurement results using statistical inference techniques and reconstruct the density matrix.

Several key aspects of the tQST protocol warrant discussion. The resources required to complete the experiment are predetermined once the threshold is set in the tQST protocol. In contrast, adaptive approaches select each measurement based on the outcome of the previous one[17,18]. tQST does not make any prior assumptions about the state, unlike some other methods that reduce the number of measurements or improve scaling by assuming a specific structure of the quantum state[5,19]. The threshold t serves to control the resources required for the protocol, such as the time needed for the measurements and the computational power for data processing. By choosing $t > 0$, fewer resources may be needed compared to QST. The threshold t can be set by the user based on available resources. However, tQST suggests that the reduction in measurements is particularly significant for sparse density matrices. To relate t to matrix sparsity, we derive a formula for t based on the initial measurements, i.e., the diagonal elements of the density matrix.

To this end, we employ the Gini index[20]. Given $\underline{c} = \left[c_{(1)}, c_{(2)}, \ldots, c_{(N)}\right]$ where $c_{(1)} \leq c_{(2)} \leq \cdots \leq c_{(N)}$ and $c_{(i)} \geq 0 \; \forall \, i$, the Gini index is defined as:

$$\mathrm{GI}(\boldsymbol{c}) = 1 - 2\sum_{\mathrm{k}=1}^{\mathrm{N}} \frac{\mathrm{c_k}}{\| \boldsymbol{c} \|_1} \left(\frac{\mathrm{N} - \mathrm{k} + \frac{1}{2}}{\mathrm{N}} \right), \tag{1}$$

where $\| \boldsymbol{c} \|_1 = \sum_{i=1}^{N} c_i$ identifies the usual Euclidean 1-norm. It holds $0 \leq \mathrm{GI}(\boldsymbol{c}) \leq 1 - 1/\mathrm{N}$, where the lower bound is attained where all the $c_{(i)}$ are equal, and the higher bound denotes maximum inequality. We adapt this definition to make the Gini index a suitable threshold for tQST. Based on the protocol, the relevant vector for computing the Gini index is the diagonal of the density matrix, where $N = 2^n$. The threshold is then set as:

$$t = \| \boldsymbol{\rho} \|_1 \, \frac{\mathrm{GI}(\boldsymbol{\rho})}{2^n - 1}, \tag{2}$$

with $\boldsymbol{\rho} = \left(\rho_{11}, \rho_{22}, \ldots, \rho_{NN}\right)$.

Experimental apparatus

The experimental setup comprises a state-of-the-art hybrid photonic architecture, interconnecting a diverse array of technologies[21] and tailored for photon-based multi-photon experiments[22,23]. More specifically, it comprises three subsequent stages, as depicted in Fig. 2. Namely, the photon resources are generated via a single-photon source based on quantum-dot (QD) technology[24–27], excited at a repetition rate of 158 MHz in the resonance fluorescence (RF) regime[25,28–31]. To quantify the quality of the single-photons emitted by the QD, we measure both the second-order autocorrelation $g^{(2)}(0)$ and the Hong–Ou–Mandel interference visibility V_{HOM} through standard correlation experiments. With the QD source employed in the experiment, we typically register values of $g^{(2)}(0) \sim 0.01$ and $V_{\mathrm{HOM}} \sim 0.90$. Then, a time-to-spatial demultiplexing module (DMX) based on an acousto-optical modulator[22,23,32–34] converts the initial train of single photons, emitted at a fixed time interval, into sets of photons distributed in several spatial modes. This procedure permits to generate a multi-photon resource, which can be injected into the input ports of the experiment. The pairwise indistinguishability between the photons comprising the generated four-photon state is guaranteed by finely tuned free-space delay lines and polarization paddle controllers. Specifically, temporal indistinguishability is ensured by finely tuning—on the millimeter scale—the position of the internal couplers of the DMX device while tracking the visibility of standard HOM interference experiments carried out on the integrated device. The multi-photon states generated with such an approach are then injected into an 8-mode fully-reconfigurable integrated photonic processor. Specifically, the present device was fabricated (see Methods) via the femtosecond laser-writing technique[35], and its internal structure is based on an interferometric mesh of 28 Mach–Zehnder unit cells, acting as Reconfigurable Beam Splitter (RBS), arranged according to the universal rectangular geometry described in ref. 36. Moreover, the integrated processor employed here features polarization-independent operation[37]. Its reconfigurability, induced by thermal-phase shifters[38–42], is suitably controlled via current controllers which can be set to implement a given chosen unitary transformation U[37]. This requires the knowledge of the current-optical phase response of the device, which can be done via suitable calibration procedures. As reported in the "Methods", with our calibrated device we reach an average moduli fidelity of 0.991 computed over randomly drawn Haar random matrices. Finally, at the output of the setup, the photons are collected from the integrated processor and then sent to a suitable detection system comprising high-efficiency superconducting nanowire single-photon detectors (SNSPDs), paired with a time-to-digital converter (TDC) used to discriminate and register n-fold coincidence events.

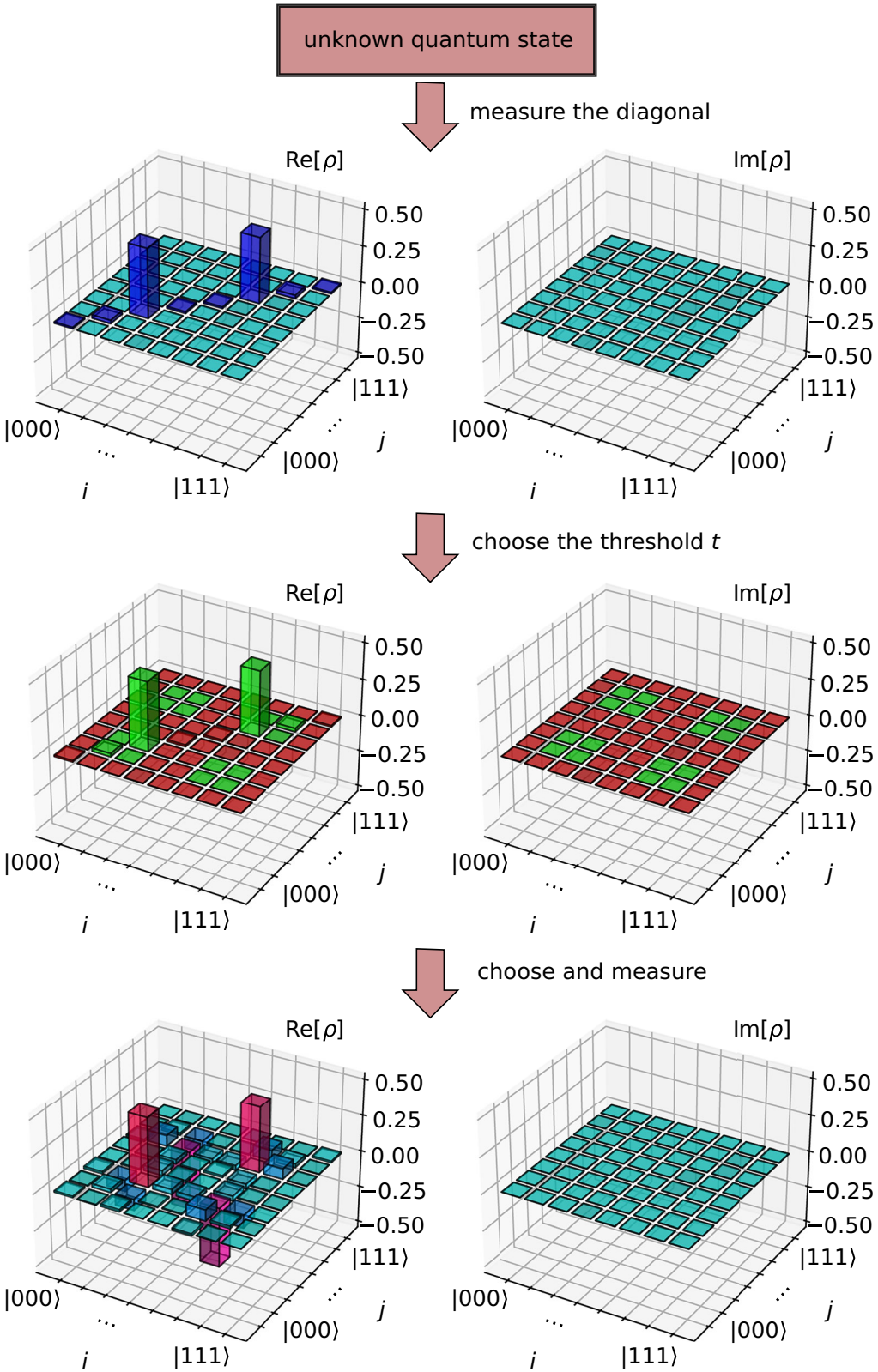

Fig. 1 | Conceptual visualization of the tQST protocol. Starting from an unknown quantum state, the protocol requires reconstructing the diagonal elements ρ_{ii} of the density matrix, which is done by measuring the state in the computational basis (upper panel, blue entries). Then, after a threshold t is appropriately set, the protocol chooses the projectors to be measured to gain information only on those off-diagonal elements ρ_{ij} corresponding to the condition $\sqrt{\rho_{ii}\rho_{jj}} \geq t$ (middle panel, green entries). From those measurements the density matrix can be then reconstructed via maximum likelihood (lower panel).

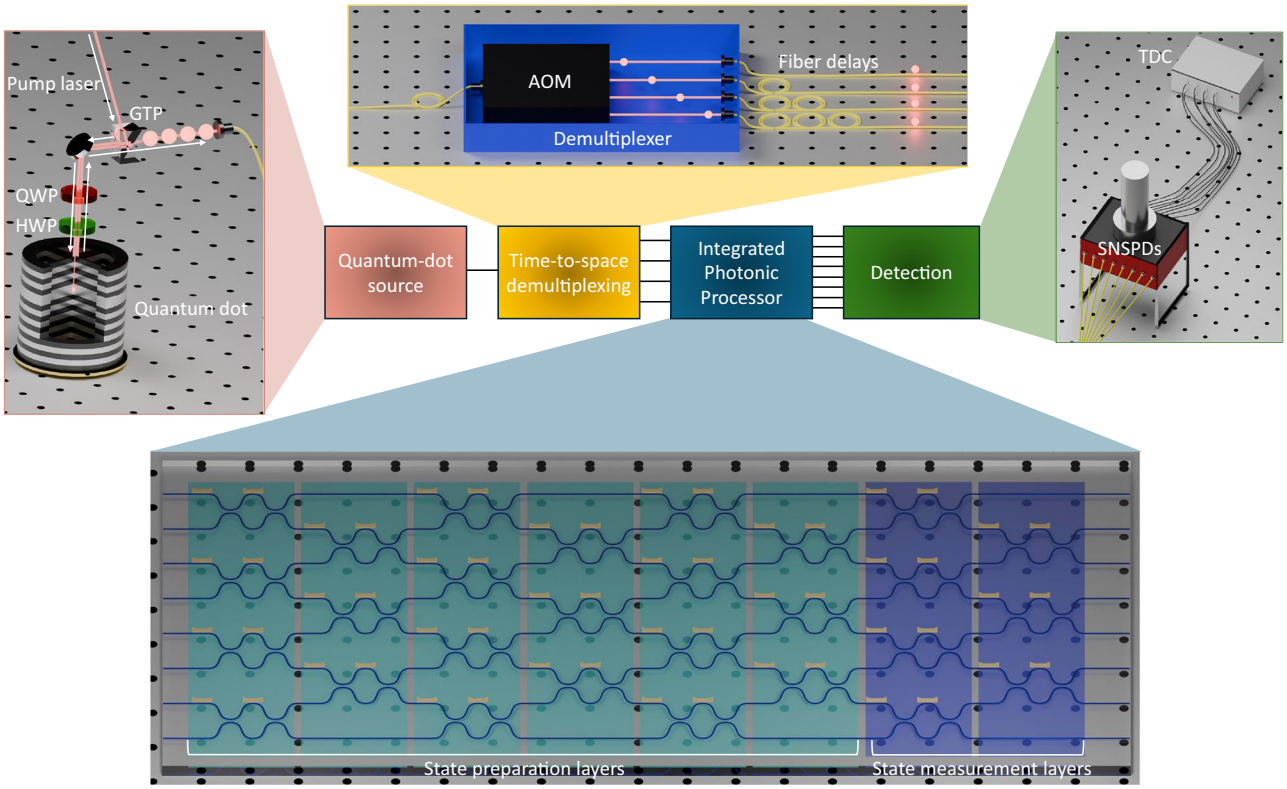

Fig. 2 | Architecture of the hybrid-photonic platform employed in the experiment. The experimental apparatus, based on a hybrid approach, has been used to generated multi-qubit states and reconstruct them via the tQST technique. A pulsed laser, manipulated with a pulse-shaping stage, is used to excite a QD single-photon source employing a resonance fluorescence (RF) optical excitation technique, comprising a Glan-Thompson polarizer (GTP), a half-wave plate (HWP) and a quarter-wave plate (QWP). Then, the single-photon stream emitted by the QD source is interfaced with the demultiplexing module, based on an acousto-optic modulator (AOM), in order to obtain the multi-photon state required for the implementation of multi-photon protocols. The output resource is then interfaced with an 8-mode fully-reconfigurable integrated photonic processor, fabricated via the femtosecond laser-writing technology, with internal structure allowing for universal operation. The first six layers (cyan) of RBSs are used to perform the state generation process in dual rail encoding, while the remaining two layers (blue) are used to measure the qubits in different bases. At the output of the setup, photon detection is carried out via superconducting-nanowire single-photon detectors (SNSPDs). Photon detection events, corresponding to n-fold coincidences, are registered via a time-to-digital converter (TDC).

Experimental results

Hereafter, we will present the results of the photonic experiment aiming to verify and validate the tQST technique[14], by analyzing different classes of states, corresponding to different level of sparsities of the density matrices. The results are benchmarked by considering the reconstruction via the tQST approach, with respect to QST which in our case is implemented via tQST with $t = 0$. The latter method uses 4^n projectors, chosen to be a tomographically-complete set[1]. We will thus refer hereafter to tQST with threshold $t = 0$ as QST.

Quantum states are generated in the photon path degree of freedom by harnessing linear optics elements, such as beam splitters and phase shifters, and considering n-fold coincidence events measured in post-selection on a subset of all possible combinations of n photons in m modes. Namely, qubit states are encoded via the *dual rail logic*[43] in the photon spatial modes. Thus, the generation of a n-qubit quantum state is obtained non-deterministically by considering an optical interferometer with an even number $m = 2n$ of modes as split into n dual rails, that is, adjacent pairs of spatial modes labeled with states $|0\rangle$ and $|1\rangle$ from top to bottom (see Fig. 2). Overall, when n photons are injected in the circuit, only the output combinations of photons distributed over the m modes, such that each dual rail is occupied by one and only one photon, are considered valid for state generation, while the others are discarded via a post-selection process.

Controlled generation of the n-qubit state and its subsequent reconstruction via tomographic measurements both take place in the aforementioned reconfigurable integrated photonic processor. As shown in Fig. 2 and in Supplementary Note 1, the first six layers of the interferometer are suitably configured to generate a chosen state. In such a view, the generation of a n-qubit state is obtained by mapping an initial n-photon state, via a suitable linear optical transformation, into a set of $2n$ modes and by applying a suitable post-selection procedure upon the detection of an n-photon coincidence event in mode combinations satisfying the dual rail logic. Conversely, the remaining two layers of the circuit are dedicated to the implementation of measurement projectors. More specifically, this relies on the possibility of implementing any arbitrary single-qubit transformation via a single elementary cell. Thus, by appropriately programming the transformation of a RBS acting on the two modes of each qubit, it is possible to implement any projective measurement on the output state. By applying the appropriate sequence of measurements according to the chosen reconstruction algorithm (either QST or tQST in this experiment), one can measure the observables needed to retrieve the initial quantum state.

The main figure of merit to quantify the efficacy of the tQST approach is given by the fidelity between the density matrix derived using tQST and the one obtained via the QST procedure ($\mathcal{F}_{0,t}$). This parameter corresponds to the overlap between the two reconstructions, and thus quantifies the amount of information that is lost by reducing the number of projectors via the tQST approach. Values of $\mathcal{F}_{0,t}$ close to one highlight that the tQST method provides an effective reconstruction of the state. A second set of relevant parameters are the purities $\mathcal{P}_0$ and $\mathcal{P}_t$ of the reconstructed states, where the state purity of a quantum state ρ is defined as $\mathrm{Tr}(\rho^2)$. The purity $\mathcal{P}_0$ represents the intrinsic value for the reconstructed state, which is due to the different noise sources in the apparatus. Additionally, evaluation of $\mathcal{P}_t$ and its comparison with $\mathcal{P}_0$ permits to verify how the purity of the reconstructed state is affected by the reduced number of projectors. Finally, the remaining relevant parameter is the fidelity between the density matrix

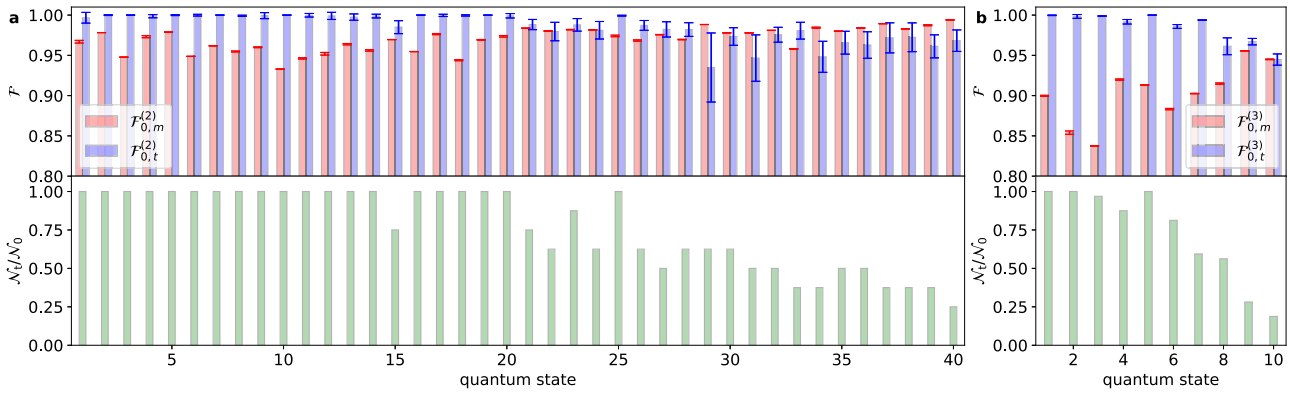

Fig. 3 | Benchmarking the tQST procedure through 2- and 3-qubit quantum state reconstruction. The tQST approach is tested by generating and analyzing a set of quantum states with equally spaced Gini index, ranging between its minimum and maximum possible value. **a** Scenario with $n = 2$ qubits, tested with 40 different states. **b** Scenario with $n = 3$ qubits, tested with 10 different states. In the upper plots, we report the fidelities $\mathcal{F}^{(n)}_{0,m}$ (with $n = 2, 3$) between the state reconstructed via QST and the theoretical model taking into account experimental imperfections (red bars), and the fidelities $\mathcal{F}^{(n)}_{0,t}$ (with $n = 2, 3$) between the state reconstructed via QST and tQST choosing the threshold according to the Gini index (blue bars). In the lower plots, we report the ratio $\mathcal{N}_t/\mathcal{N}_0$ (green bars) between the number of projectors $\mathcal{N}_t$ selected to be measured by the tQST approach with threshold according to Eq. 2, and the number of projectors $\mathcal{N}_0$ corresponding to the QST approach. The states are ordered on the x-axis according to the associated Gini indexes. Error bars on the fidelity estimations are computed by standard bootstrapping techniques, considering the standard deviation of the fidelities computed from a set of 250 independent solutions to the state reconstruction problem. Each solution is obtained by initializing from the experimental data the optimization algorithm with different initial seeds, that is, by inserting a different guesses for the starting point of the maximum likelihood algorithm.

derived using the QST procedure and the expected state from the apparatus ($\mathcal{F}_{0,m}$). This expected state is obtained via numerical simulations that consider the main noise effects in the apparatus, due to non-ideal single-photon emission from the QD source[22,23,33,34], to losses and to an imperfect dialling of the unitary matrix on the integrated photonic processor. The noise effects that we consider are related to (i) a non-zero multi-photon emission probability from the QD source, (ii) a degree of partial distinguishability between the photons and iii) directional couplers of the elementary cell with a splitting ratio different from 50:50 (more details can be found in Supplementary Note 2). The parameters related to the different effects have been estimated by independent measurements. More specifically, noise source (i) is characterized by a standard measurement of the second-order autocorrelation via a Hanbury Brown–Twiss interferometer. Conversely, partial distinguishability (ii) can be estimated through measurement of the Hong–Ou–Mandel visibilities V_{HOM} between the photons emitted at different times. Finally, the splitting ratios of the directional couplers iii) have been retrieved during the circuit calibration procedure.

As a first step, we have implemented experimentally the tQST technique on a set of states for $n = 2$ and $n = 3$ qubits. More specifically, we have generated a set of random states for each dimension, and selected a subset of 40 states for $n = 2$, and 10 states for $n = 3$, where each set is characterized by equally-spaced values of the Gini index, from the minimum to the maximum value, calculated on the diagonal elements of the density matrices. This approach allows to test the performances of the tQST method by considering states covering uniformly the full range of possible degrees of sparsity in the diagonal. The chosen states are generated, according to the procedure above, in the dual rail logic, by using n input photons and a portion of the circuit composed of $m = 2n$ modes. For each value of the number of qubits, a number of RBSs equal to $N_{\mathrm{RBS}} = m(m-1)/2$, which constitute a m-mode universal multiport interferometer, are exploited in the state preparation stage (more details on the layout are found in Supplementary Note 1). Population and coherence elements of the density matrices are processed via the measurement layers, comprising single-qubit projectors.

The results of the state reconstruction process with both QST and tQST are shown in Fig. 3. For each analyzed state we report the fidelity $\mathcal{F}^{(n)}_{0,t}$ between the density matrices obtained with the two approaches, and perform a joint analysis with the ratio $\mathcal{N}_t/\mathcal{N}_0$ between the number of projectors used by tQST ($\mathcal{N}_t$) and the ones used by QST ($\mathcal{N}_0$). Here, the reconstruction with the tQST method is performed by choosing the threshold according to the Gini index [Eq. (2)]. We note that the GI threshold is evaluated only considering the diagonal elements of the density matrix, while the set of projectors to be measured is later determined by the tQST protocol according to the procedure discussed above. We observe that, for states with the lowest sparsity values, the two techniques coincide given that the tQST approach requires measuring a tomographically-complete set of 4^n projectors. When measuring states with increasing sparsity in the diagonal elements, the tQST starts to be advantageous due to the measurement of a progressively lower number of projectors, as shown in the bottom panels of Fig. 3. The obtained quality in the reconstructions for all states shows that tQST is effective in reducing the number of projectors while having only a very limited loss of information with respect to the QST approach, since all fidelities are found to be $\mathcal{F}^{(n)}_{0,t} > 0.935$. Such advantage in reducing the number of projectors becomes more pronounced when increasing the state dimensionality, given the exponential increase in the number of measurements required by QST. As a final note, we observe that the reconstructed states show a good agreement with the theoretical expectations from the model (see also Supplementary Note 3 for additional comparisons), as quantified by the average fidelities $\langle \mathcal{F}^{(2)}_{0,m} \rangle = 0.969 \pm 0.014$ for the 2-qubit scenario, and $\langle \mathcal{F}^{(3)}_{0,m} \rangle = 0.903 \pm 0.035$, for the 3-qubit case.

As a subsequent step to test the tQST approach, we have analyzed its application to reconstruct specific maximally-entangled states characterized by a density matrix comprising a large number of zero-valued elements. In this case, the tQST method is expected to maximize the advantage with respect to the QST approach. Indeed, in a noiseless scenario a large number of projectors correspond to zero-valued elements, and the protocol does not require their measurement to reconstruct the state. We have then tested different maximally-entangled states, such as $|\Psi^+\rangle = (|01\rangle + |10\rangle)/\sqrt{2}$ for $n = 2$ qubits, $|\mathrm{GHZ}_3\rangle = (|010\rangle + |101\rangle)/\sqrt{2}$ and $|\mathrm{W}_3\rangle = (|100\rangle + |010\rangle + |001\rangle)/\sqrt{3}$ for $n = 3$ qubits, and $|\mathrm{GHZ}_4\rangle = (|0101\rangle + |1010\rangle)/\sqrt{2}$ for $n = 4$ qubits. The Bell state and the GHZ states are generated by following the post-selected approach of ref. 34, while the W state is generated by exploiting the full reprogrammability of the device (more details on the configuration for the generation layout are found in Supplementary Note 1).

The results for the reconstructed density matrices with the two methods, and their comparison with the model of the apparatus, are shown in Fig. 4 (complementary analyses are reported in Supplementary Note 3). We observe that, for all states, the reconstructed states with the tQST approach, using the Gini index to choose the threshold, are close to those

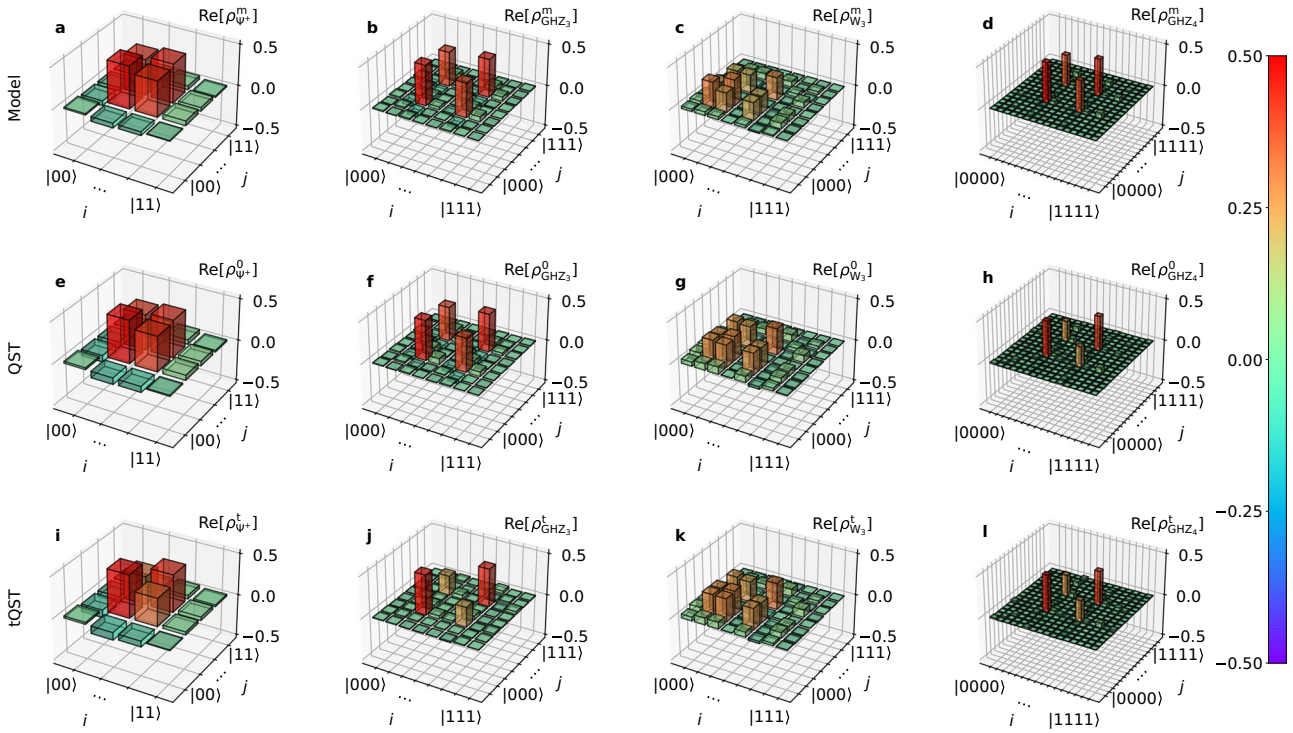

Fig. 4 | Results of the state reconstruction process for maximally-entangled states. Real part of the density matrices for the different tested maximally-entangled states, namely (from left to right) $|\Psi^+\rangle$ for $n = 2$, $|GHZ_3\rangle$ and $|W_3\rangle$ for $n = 3$ and $|GHZ_4\rangle$ for $n = 4$. In the first row (panels **a**–**d**) we report the expected density matrices (ρ_α^m) estimated from the model taking into account experimental imperfections. The second row (panels **e**–**h**) reports the corresponding experimentally reconstructed density matrices (ρ_α^0) via the QST approach, while the third row (panels **i**–**l**) reports the density matrices (ρ_α^t) retrieved via the tQST approach with threshold chosen according to the Gini index. The index α labels the states as $\alpha = \Psi^+$, GHZ_3, W_3, GHZ_4. On the right part of the figure, we report the colormap for the density matrix bars, equal for all plots **a**–**l**.

Table 1 | Reconstruction of maximally-entangled states

State	$\mathcal{N}_0$	$\mathcal{N}_t$	$\mathcal{F}_{0,t}^{(\alpha)}$
$\|\Psi^+\rangle$	16	6	0.94 ± 0.03
$\|GHZ_3\rangle$	64	10	0.84 ± 0.05
$\|W_3\rangle$	64	32	0.9833 ± 0.0007
$\|GHZ_4\rangle$	256	66	0.948 ± 0.005

Values of the number of projectors $\mathcal{N}_t$ used by tQST with a value of the threshold chosen according to the Gini index, of the number of projectors $\mathcal{N}_0$ required by QST, and of the fidelities $\mathcal{F}_{0,t}^{(\alpha)}$ between the two reconstruction techniques. The index α labels the states as $\alpha = \Psi^+$, GHZ_3, W_3, GHZ_4. The reported fidelities and associated errors are computed over 250 independent solutions to the state reconstruction problem.

obtained with QST. A more detailed analysis on the performances can be found in Table 1 and in Fig. 5, where we have analyzed tQST by further using different number of projectors $\mathcal{N}$ with respect to the one indicated by the Gini threshold. We start by analyzing the fidelity between QST and tQST $\mathcal{F}_{0,t}^{(\alpha)}$ as a function of the number of projectors $\mathcal{N}$, with $\alpha = \Psi^+$, GHZ_3, W_3, GHZ_4. We observe that, for all states, the initial reduction of the number of projectors in a regime above the value identified by the Gini index is accompanied by a small loss of information. For the $|\Psi^+\rangle$ state, we observe that setting the threshold to those identified by the Gini index captures the correct boundary where the minimal number of projectors is measured. Indeed, we observe that further reducing this value corresponds to a larger loss of information. For the $|GHZ_3\rangle$ state, this approach sets the threshold for the number of projectors very close to the boundary, and the obtained value of the fidelity can be increased up to ~0.95 by adding a very limited (≤10) number of additional projectors. Conversely, for the $|W_3\rangle$ and $|GHZ_4\rangle$ states we observe that setting the threshold to the one provided by the Gini index [Eq. (2)] corresponds to a slightly conservative choice, given that it is still possible to perform a further moderate reduction in the number of projectors without adding significant loss of information on the state. The same trend is confirmed by observing the purity of the reconstructed states with the tQST approach. For this parameter, the effect of removing an exceeding amount of projectors with respect to those indicated by the Gini index is found in a significant reduction of the reconstructed matrix purity, since not enough information was collected to properly estimate this parameter. We also observe that the purity of the reconstructed density matrices decreases with the size of the system. This is not due to the reconstruction method, but it depends on the increased impact of experimental imperfections in the state generation process when the number of photons increases. As a final note, we observe that the tQST approach with threshold at the Gini index chooses a number of projectors which is different than the one expected for the corresponding noiseless states. Indeed, the presence of experimental noise adds other non-zero values in the diagonal elements, which then results in the need to measure additional projectors than those required for an ideal state.

Discussion

In this manuscript, we have tested experimentally the application of the tQST approach in a hybrid photonic platform, verifying its application on states of up to $n = 4$ qubits. The method is shown to provide an accurate reconstruction of unknown quantum states with different levels of sparsity in the density matrix, as testified by the fidelities achieved with the reconstructed states with respect to those obtained by measuring a complete set of projectors. The advantage is found to be more pronounced for states having different elements with small (or zero) values in the density matrix, such as specific classes of maximally-entangled states which are at the basis of several quantum information protocols. According to the detected coincidence rates and considering that in our platform multiple projectors

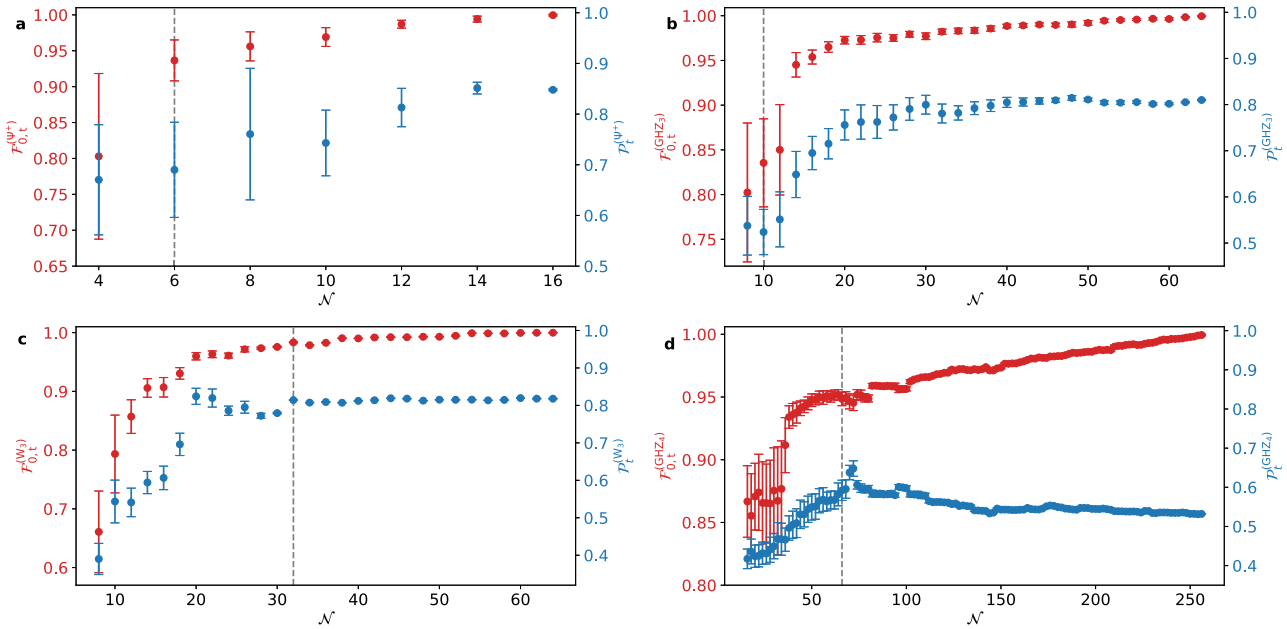

Fig. 5 | Reconstruction of maximally-entangled states. Red points: plots of the fidelities ($\mathcal{F}^{(\alpha)}_{0,t}$) between the state reconstructed via QST, and the state reconstructed via tQST for different values of the number projectors $\mathcal{N}$, obtained by progressively lowering the value of the threshold t. Blue points: corresponding purities ($\mathcal{P}^{(\alpha)}_{t}$) for the states reconstructed via tQST as a function of $\mathcal{N}$. The index α labels the states as $\alpha = \Psi^+, \mathrm{GHZ}_3, \mathrm{W}_3, \mathrm{GHZ}_4$. **a** Plots for state $|\Psi^+\rangle$. **b** Plots for state $|\mathrm{GHZ}_3\rangle$. **c** Plots for state $|\mathrm{W}_3\rangle$. **d** Plots for state $|\mathrm{GHZ}_4\rangle$. In all plots, the vertical dashed lines correspond to the number of projectors obtained using the threshold computed from the Gini index [Eq. (2)]. Error bars on the fidelity and purity estimations are computed by standard bootstrapping techniques, considering the standard deviation of the fidelities computed from a set of 250 independent solutions to the state reconstruction problem. Each solution is obtained by initializing from the experimental data the optimization algorithm with different initial seeds, that is, by inserting a different guesses for the starting point of the maximum likelihood algorithm.

corresponding to the same basis are measured simultaneously in a single setting, application of the tQST method to the $n = 4$ GHZ state led to a reduction in the time to measure the required projectors to approximately ~7.5 h with respect to ~40.5 h to implement QST. The obtained results thus show the effectiveness of the approach on a photonic platform, and open new perspectives in its application in larger systems.

Methods

Reconfigurable integrated photonic processor

The integrated photonic processor was fabricated using the femtosecond laser-writing (FLW) platform[35]. This technique has several peculiar properties, such as permitting to write waveguides at speeds of several centimeters per second, enabling the fabrication of complex circuits with throughputs as high as thousands per day. Furthermore, the platform benefits from minimal post-processing and no need of advanced cleanroom facilities, which contribute to a scalable and cost-effective manufacturing process.

The processor features a waveguide layout based on a rectangular mesh of Mach–Zehnder interferometers (MZIs)[36], enabling the implementation of arbitrary linear transformations on eight input and output modes. Each MZI unit consists of two sequential directional couplers and includes two thermal phase shifters (i.e., resistive microheaters): one for tuning the relative phase between the modes and the other for adjusting the output intensity distribution.

Waveguides were optimized for single-mode operation at wavelengths compatible with quantum dot single-photon sources (i.e., 927 nm) and inscribed using a multi-pass technique on Corning EAGLE XG boro-aluminosilicate glass substrate as reported in ref. 34. The fabrication process is followed by a thermal annealing step to relieve stresses introduced during the irradiation and to minimize optical losses[44].

Microheaters were fabricated using a two-step photolithography process, followed by the selective etching of chromium (resistive elements) and copper (metal connections)[41]. Additional microstructuring of the chip surface, namely laser ablation of deep thermal isolation trenches around the microheaters, was implemented to enhance power efficiency and reduce thermal crosstalk[40]. Each thermal phase shifter dissipates, on average, a maximum of 38 mW when inducing a full 2π phase shift. However, during typical operation (i.e., when the device is configured with varying phases), the total power consumption across all microheaters stays below 1.5 W, ensuring compatibility with thermo-electric cooling. Regarding reconfiguration speed, the 10–90% rise/fall time of a single MZI is approximately 50 ms. To mitigate the effects of slow thermal crosstalk, before each new measurement, we conservatively introduced a waiting time of several hundred milliseconds when applying new current settings. This additional delay, however, does not block the typical data acquisition pipeline of a quantum experiment, since, to gather sufficient photon statistics, the data collection takes place on a much longer time scale.

The device has a footprint of 15 mm × 85 mm and features input/output fiber arrays that are directly glued to the chip to facilitate optical interfacing. Waveguide fan-in and fan-out structures were designed and fabricated to enable a smooth transition from the 127 μm fiber pitch to the 80 μm inter-waveguide spacing used within the circuit. The curvature radius of the waveguides is 20 mm, selected as the minimum value that does not introduce additional losses (i.e., bending losses).

The overall fiber-to-fiber insertion loss is below 3 dB, corresponding to a total transmission of approximately 50%. This value includes both propagation losses within the integrated circuit and coupling losses at the chip facets. Considering that the coupling losses with fiber arrays is approximately 0.5 dB per facet, the insertion losses attributable to the integrated photonic processor itself is about 2 dB. This corresponds to an average optical loss of 0.25 dB per MZI layer.

Finally, the processor was calibrated by using a coherent light source at the design wavelength of 927 nm as described in ref. 37. The calibration procedure consists in characterizing the relation:

$$\phi = \phi_0 + \alpha I^2, \tag{3}$$

where the phase vector ϕ is linearly related to the square of the current vector I through the tuning matrix coefficient α and the static phase vector ϕ_0. This

approach allows us to effectively account for thermal crosstalk among the phase shifters. Nonlinear effects are neglected, as they are not significant within the operating temperature range of the phase shifters. The processor was operated using multichannel driving electronics capable of setting the electrical currents with a precision of approximately 1 μA, corresponding to a phase resolution better than 1 mrad over the full tuning range from 0 to 2π. The calibration accuracy was assessed by implementing 100 Haar-randomly selected unitary transformations and evaluating the amplitude fidelity using the expression:

$$\mathcal{F}_{\mathrm{ampl}}(U_{\mathrm{set}}, U_{\mathrm{exp}}) = \frac{1}{N}\mathrm{Tr}(|U_{\mathrm{set}}^{\dagger}||U_{\mathrm{exp}}|). \quad (4)$$

where $N = 8$ is the number of modes, U_{exp} is the experimentally reconstructed matrix (moduli only) and U_{set} is the target unitary. The resulting average fidelity was ~0.991.

Data availability

Data sets generated during the current study are available from the corresponding author on reasonable request.

Code availability

The code that support the findings of this study are available from the corresponding authors upon reasonable requests.

Received: 19 May 2025; Accepted: 14 September 2025;
Published online: 07 November 2025

References

1. James, D. F., Kwiat, P. G., Munro, W. J. & White, A. G. Measurement of qubits. *Phys. Rev. A* **64**, 052312 (2001).
2. Thew, R. T., Nemoto, K., White, A. G. & Munro, W. J. Qudit quantum-state tomography. *Phys. Rev. A* **66**, 012303 (2002).
3. D'Ariano, G. M., Paris, M. G. & Sacchi, M. F. Quantum tomography. *Adv. Imaging Electron Phys.* **128**, 205 (2003).
4. Altepeter, J. B., Jeffrey, E. R. & Kwiat, P. G. Photonic state tomography. *Adv. At., Mol., Opt. Phys.* **52**, 105 (2005).
5. Gross, D., Liu, Y.-K., Flammia, S. T., Becker, S. & Eisert, J. Quantum state tomography via compressed sensing. *Phys. Rev. Lett.* **105**, 150401 (2010).
6. Flammia, S. T., Gross, D., Liu, Y.-K. & Eisert, J. Quantum tomography via compressed sensing: error bounds, sample complexity and efficient estimators. *N. J. Phys.* **14**, 095022 (2012).
7. Tonolini, F., Chan, S., Agnew, M., Lindsay, A. & Leach, J. Reconstructing high-dimensional two-photon entangled states via compressive sensing. *Sci. Rep.* **4**, 6542 (2014).
8. Blume-Kohout, R. Optimal, reliable estimation of quantum states. *N. J. Phys.* **12**, 043034 (2010).
9. Lu, H.-H. et al. Quantum interference and correlation control of frequency-bin qubits. *Optica* **5**, 1455 (2018).
10. Lu, H.-H. et al. Bayesian tomography of high-dimensional on-chip biphoton frequency combs with randomized measurements. *Nat. Commun.* **13**, 4338 (2022).
11. Aaronson, S. Shadow tomography of quantum states. In *Proceedings of the 50th Annual ACM SIGACT Symposium on Theory of Computing* 325–338 (ACM Press, 2018).
12. Huang, H.-Y., Kueng, R. & Preskill, J. Predicting many properties of a quantum system from very few measurements. *Nat. Phys.* **16**, 1050 (2020).
13. Struchalin, G., Zagorovskii, Y. A., Kovlakov, E., Straupe, S. & Kulik, S. Experimental estimation of quantum state properties from classical shadows. *PRX Quantum* **2**, 010307 (2021).
14. Binosi, D., Garberoglio, G., Maragnano, D., Dapor, M. & Liscidini, M. A tailor-made quantum state tomography approach. *APL Quantum* **1**, 036112 (2024).
15. Wang, J., Sciarrino, F., Laing, A. & Thompson, M. G. Integrated photonic quantum technologies. *Nat. Photonics* **14**, 273 (2020).
16. Giordani, T., Hoch, F., Carvacho, G., Spagnolo, N. & Sciarrino, F. Integrated photonics in quantum technologies. *Riv. Nuovo Cim.* **46**, 71 (2023).
17. Ahn, D. et al. Adaptive compressive tomography with no a priori information. *Phys. Rev. Lett.* **122**, 100404 (2019).
18. Ahn, D. et al. Adaptive compressive tomography: a numerical study. *Phys. Rev. A* **100**, 012346 (2019).
19. Baumgratz, T., Gross, D., Cramer, M. & Plenio, M. B. Scalable reconstruction of density matrices. *Phys. Rev. Lett.* **111**, 020401 (2013).
20. Hurley, N. & Rickard, S. Comparing measures of sparsity. *IEEE Trans. Inf. Theory* **55**, 4723 (2009).
21. Elshaari, A. W., Pernice, W., Srinivasan, K., Benson, O. & Zwiller, V. Hybrid integrated quantum photonic circuits. *Nat. photonics* **14**, 285 (2020).
22. Rodari, G. et al. Semi-device independent characterization of multiphoton indistinguishability. *Phys. Rev. X* **6**, 020340 (2025).
23. Rodari, G. et al. Experimental observation of counter-intuitive features of photonic bunching. Preprint at https://arxiv.org/abs/2410.15883 (2024).
24. Michler, P. *Quantum Dots for Quantum Information Technologies*, Vol. 237 (Springer, 2017).
25. Senellart, P., Solomon, G. & White, A. High-performance semiconductor quantum-dot single-photon sources. *Nat. Nanotechnol.* **12**, 1026 (2017).
26. Heindel, T., Kim, J.-H., Gregersen, N., Rastelli, A. & Reitzenstein, S. Quantum dots for photonic quantum information technology. *Adv. Opt. Photonics* **15**, 613 (2023).
27. Esmann, M., Wein, S. C. & Antón-Solanas, C. Solid-state single-photon sources: recent advances for novel quantum materials. *Adv. Funct. Mater.* **34**, 2315936 (2024).
28. Somaschi, N. et al. Near-optimal single-photon sources in the solid state. *Nat. Photonics* **10**, 340 (2016).
29. Ollivier, H. et al. Reproducibility of high-performance quantum dot single-photon sources. *ACS Photonics* **7**, 1050 (2020).
30. Nowak, A. et al. Deterministic and electrically tunable bright single-photon source. *Nat. Commun.* **5**, 3240 (2014).
31. Gazzano, O. et al. Bright solid-state sources of indistinguishable single photons. *Nat. Commun.* **4**, 1425 (2013).
32. Hansen, L. M. et al. Single-active-element demultiplexed multi-photon source. *Opt. Quantum* **1**, 1 (2023).
33. Pont, M. et al. Quantifying n-photon indistinguishability with a cyclic integrated interferometer. *Phys. Rev. X* **12**, 031033 (2022).
34. Pont, M. et al. High-fidelity four-photon GHZ states on-chip. *npj Quantum Inf.* **10**, 50 (2024).
35. Corrielli, G., Crespi, A. & Osellame, R. Femtosecond laser micromachining for integrated quantum photonics. *Nanophotonics* **10**, 3789 (2021).
36. Clements, W. R., Humphreys, P. C., Metcalf, B. J., Kolthammer, W. S. & Walmsley, I. A. Optimal design for universal multiport interferometers. *Optica* **3**, 1460 (2016).
37. Pentangelo, C. et al. High-fidelity and polarization-insensitive universal photonic processors fabricated by femtosecond laser writing. *Nanophotonics* **13**, 2259 (2024).
38. Flamini, F. et al. Thermally reconfigurable quantum photonic circuits at telecom wavelength by femtosecond laser micromachining. *Light Sci. Appl.* **4**, e354 (2015).
39. Ceccarelli, F., Atzeni, S., Prencipe, A., Farinaro, R. & Osellame, R. Thermal phase shifters for femtosecond laser written photonic integrated circuits. *J. Lightwave Technol.* **37**, 4275 (2019).
40. Ceccarelli, F. et al. Low power reconfigurability and reduced crosstalk in integrated photonic circuits fabricated by femtosecond laser micromachining. *Laser Photonics Rev.* **14**, 2000024 (2020).
41. Albiero, R. et al. Toward higher integration density in femtosecond-laser-written programmable photonic circuits. *Micromachines* **13**, 1145 (2022).

42. Ceccarelli, F. et al. Integrated thermo-optic phase shifters for laser-written photonic circuits operating at cryogenic temperatures. *J. Phys.: Photonics* **6**, 045023 (2024).
43. Kok, P. et al. Linear optical quantum computing with photonic qubits. *Rev. Mod. Phys.* **79**, 135 (2007).
44. Corrielli, G. et al. Symmetric polarization-insensitive directional couplers fabricated by femtosecond laser writing. *Opt. Express* **26**, 15101 (2018).

Acknowledgements

This work is supported by PNRR MUR project PE0000023-NQSTI (Spoke 1, Spoke 4, and Spoke 7) and by the European Union's Horizon Europe research and innovation program under EPIQUE Project (Grant Agreement No. 101135288). Fabrication of the femtosecond laser-written integrated circuit was partially performed at PoliFAB, the micro and nano-fabrication facility of Politecnico di Milano (https://www.polifab.polimi.it). F.C. and R.O. wish to thank the PoliFAB staff for the valuable technical support.

Author contributions

E.C., D.M., G.R., G.G., D.B., N.S., M.D., M.L., and F.S. conceived the idea. R.A., N.D.G., F.C., G.C., and R.O. fabricated the photonic chip and characterized the integrated devices using classical optics. E.C., G.R., D.P., N.S., and F.S. carried out the quantum experiments. E.C., D.M., G.R., D.P., G.G., D.B., N.S., M.D., M.L., and F.S. performed the data analysis. All the authors discussed the results and contributed to the preparation of the manuscript.

Competing interests

G.C., F.C., and R.O. are co-founders of the company Ephos (www.ephos.io). The other authors declare no competing interests.

Additional information

Supplementary information The online version contains supplementary material available at https://doi.org/10.1038/s41534-025-01111-z.

Correspondence and requests for materials should be addressed to Roberto Osellame, Maurizio Dapor, Marco Liscidini or Fabio Sciarrino.